Landslides (2018) 15:199–217
DOI 10.1007/s10346-017-0865-0
Received: 11 January 2017
Accepted: 14 July 2017
Published online: 1 August 2017

R. Tomás · A. Abellán · M. Cano · A. Riquelme · A. J. Tenza-Abril · F. Baeza-Brotons · J. M. Saval · M. Jaboyedoff

A multidisciplinary approach for the investigation of a rock spreading on an urban slope

Abstract Landslides are very complex processes controlled by multiple factors. The knowledge and characterization of these factors is essential for a comprehensive understanding of the mechanisms and kinematics of the instabilities and for an efficient design of corrective measures. The aim of this work is to combine traditional geological and geotechnical techniques with geophysical, remote sensing and forensic techniques for obtaining a whole picture of an active lateral spreading affecting the Finestrat municipality in Alicante, SE Spain. Geomorphological, geotechnical and geophysical techniques (i.e. ground penetrating radar and refraction seismic) have provided essential information about the geometry, structure and petro-physical properties of the slope. A Terrestrial Laser Scanner was used for recognizing the most important sets of discontinuities affecting the rock mass and to evaluate the activity of the landslide slope. Complementarily, a forensic analysis of the building damage completed the available datasets, yielding very useful kinematic information of the landslide. Finally, a sensitivity analysis of the stability of the rock slope has been performed considering both block toppling and block sliding models. Therefore, the multisource analysis performed in this work has allowed the identification and characterization of a complex lateral spreading, highlighting its effectiveness for a comprehensive understanding of this type of landslide.

Keywords Building damage · Deformation · LiDAR · Multidisciplinary approach · Rock spreading · Stability analysis

Introduction

Landslides are complex landscape processes controlled by a high number of geometrical, geological and geotechnical factors. Given their complexity, it is usually necessary to merge information from different sources and techniques for a comprehensive and precise understanding of the phenomenon and the later effective design of the corrective measures (Ausilio and Zimmaro 2016). The multi-technique approach, which consists of the integration of information obtained from different techniques, has been successfully applied to the study of many landslides (e.g. Ausilio and Zimmaro 2016, Crosta et al. 2014, Hürlimann et al. 2006, Mantovani et al. 2013, Merritt et al. 2014, Naudet et al. 2008, Sass et al. 2008, Travelletti et al. 2013, Travelletti and Malet 2012). As the geometry of bedrock, internal layers and sliding surface of landslides govern their mechanism and displacement pattern (Travelletti and Malet 2012), geological, hydrological, geophysical and geotechnical instrumentation for monitoring are frequently combined for the characterization of this gravitational process. This information can be classified into five groups according to Traveletti and Mallet (2012): (a) kinematic (i.e. activity and distribution of velocities), (b) geomorphologic (i.e. based on the analysis of landforms), (c) geological (i.e. to map and spatially arrange the different lithologies as well as the main structures), (d) geotechnical (i.e. to geomechanically characterize the involved lithologies) and (e) petrophysical (i.e. to provide information from the subsurface).

During recent decades, remote sensing techniques such as Laser Scanning or Light Detection and Ranging (LiDAR) and SAR Interferometry (InSAR) have also become essential tools for the study of landslides (Jaboyedoff et al. 2012). InSAR allows the measurement of small displacements over wide areas and LiDAR provides three-dimensional topographic information of the slope, providing data of high interest for the study, understanding and subsequent risk mitigation associated to the slope instabilities. The LiDAR technique allows obtaining high-resolution digital terrain models (DTMs) from acquisition distances up to thousands of meters which can be used for the detection and characterization of landslides (e.g. Palenzuela et al. 2014, Royán et al. 2014), landslide hazard and susceptibility studies (e.g. Ferrero et al. 2011, Gorsevski et al. 2015), modelling and monitoring of landslides (e.g. Heckmann et al. 2012) and rock mass characterization (e.g. Riquelme et al. 2014, Riquelme et al. 2016, Sturzenegger and Stead, 2009a, b).

Urban areas are zones of particular vulnerability to landslide damage (Alexander 1986, Mansour et al. 2011). In these areas, landslides can affect infrastructures and population placed on their depletion or accumulation zones even causing fatalities (Mansour, et al. 2011). Therefore, the location and evaluation of the landslide-induced damage is essential to understand the exposure of the infrastructures and the population to this natural hazard in order to take appropriate remedial measures and effectively respond to future events. Moreover, the study of infrastructure damage can contribute to the understanding of the causes of the landslides along with an understanding of the impact that humans have on these factors. This study is mainly performed in the field by means of the compilation and description of data, such as the materials used in construction, the type of foundation and the type of architectural details, among others (Alexander 1986).

In this paper, we present the case study of a rock spreading in Finestrat (Alicante, SE Spain) as an example of an effective multi-technical approach to understand the mechanism, kinematics and conditioning factors of the landslide. To this aim, geomorphological data, geotechnical information (i.e. geotechnical instrumentation, boreholes and laboratory tests), geophysical investigation results (i.e. seismic refraction and ground penetrating radar), forensic records and LiDAR-derived remote sensing information have been integrated and jointly analysed.

The paper is organized as follows: the general setting of the study area is detailed in the "Study area" section. The "Geological and geotechnical settings", "Geophysical surveys", "Remote sensing investigations" and "Forensic analysis of buildings" sections present the geological-geotechnical, geophysical, remote sensing and forensic information integrated in this work for the investigation of the landslide. Note that due to the large number of

techniques used in this work, the methods and the results have been combined in these sections for a simpler and clearer presentation of the information. The comprehensive interpretation of the results provided by the different techniques is described in the "Interpretation and synthesis" section, and the "Conclusions" section summarizes the main conclusions of the paper.

Study area

The study area (Fig. 1) is located in the easternmost sector of the Betic cordillera, which corresponds to the named Prebetic of Alicante. This area is characterized by the predominance of carbonatic and marly lithologies from Jurassic to Quaternary and wide gypsiferous diapiric Triassic outcrops (Colodrón and Ruíz 1978). The urban area of Finestrat, which has about 6000 inhabitants, is placed over a diapir, which is delimited to the south and west by steep slopes mainly composed by Triassic lithologies.

The municipality of Finestrat is a major tourist attraction of Alicante. Most of the urban area is placed on the crown of a steep slope with a height up to 30 m. The slope is mainly composed of massive Keuper Triassic brittle gypsums on the top of the slope with alternating layers of clay, marl and sandstones on the bottom. Gypsum rock mass instabilities (e.g. toppling and rockfall) are frequent on the whole slope as shown by the large number of fallen rock blocks accumulated along the foot of the whole slope. In fact, a large rockfall event that occurred in January 2012 disrupted the road traffic for several hours without causing personal injury. However, in the recent times, the situation has become worse as some buildings placed above the slope have been severely affected by the slope activity and thus, this problem has attracted public attention.

Climatically, the area presents typical Mediterranean weather characterized by the presence of irregular and random precipitations with severe drought periods. Mean annual cumulative precipitations of 481 mm and temperature of 16.9 °C were recorded during the period 1981–2010 (Climate-Data 2016). The drought periods range from 3 to 5 months, with few rainy days. At the end of drought periods, the autumnal heavy rainstorms can cause severe floods.

Geological and geotechnical settings

The field survey and the analysis of aerial orthophotos from 2003, 2006 and 2009 with a scale of 1:5000 as well as a 0.5-m grid digital elevation model (DEM) (GVA 2017) were used for geological and geomorphological mapping. This information was complemented by the existing lithological and geotechnical 1D information from two deep boreholes (S-1 and S-2, 39.75 and 30.30 m depth, respectively) bored in 2008 (Saval et al. 2009) and two shallow boreholes (S-1′ and S-2′, 9 m depth each) drilled in 2014 (Ayuntamiento de Finestrat 2014) (Figs. 1 and 2). Boreholes S-1 and S-2 were instrumented by means of inclinometers, and three undisturbed samples were tested in the laboratory to identify and determine the mechanical and deformational properties of the involved soils and rocks (Table 1). Complementarily, ten new geotechnical tests were performed using the three undisturbed samples taken from boreholes S-1′ and S-2′ (Table 1).

According to this information, three main lithological units were recognized in the study area by Saval et al. (2009) based on Colodrón and Ruíz (1978) (Figs. 1 and 2): anthropogenic (ml_1 and ml_2), Quaternary (Q) and Upper Triassic subunits (T_1 and T_2).

Anthropogenic Unit is composed by made land or artificial fill (ml_1) moved for construction purposes (e.g. roads embankments, urban area, etc.) and agricultural disturbances (ml_2). The Quaternary Unit (Q) is constituted by colluvial sediments composed of gravels with a clayey matrix and gypsum clasts that cover the lower part of the slopes, reaching maximum thickness on the NE sector of the study area. In the top of the slope, the thickness of this unit varies from 0.7 to 1.4 m. These units have been scarcely characterized in this study.

Two subunits can be differentiated in the Upper Triassic Unit (Table 1). The first one (T_1) consists of red and grey marls and clays with thin (centimetre thick) layers of gypsum. This level presents a low plasticity (CL-SM), medium to stiff consistency (Uniaxial compressive strength (UCS) varying from 0.2 to 1.1 MPa) and occasional layers of competent sandstones (UCS equal to 3.6 MPa). The top of this layer has been found in S-1, S-1′ and S-2′ boreholes at a depth varying from 3.7 to 13.2 m from ground surface. The second subunit (T_2), whose thickness varies from 2.6 m in S-2′ to 13.2 m in S-1, is composed by high competence massive gypsum (UCS from 0.86 to 12.40 MPa) with thin marl and sandstone intercalations. This subunit presents a "Very high" to "Extremely high" 2-cycle slake durability index (Id_2) according to Franklin and Chandra (1972).

From a structural point of view, the slope under study is mainly affected by an up to 40 m long earth fissure-oriented parallel to the slope with a predominant N110° orientation. The fissure crosses some buildings and presents apertures up to near 25 cm ("extremely wide" according to ISRM (1978)).

Some springs were recognized in five different locations of the study area during the field works developed in June 2008 (Fig. 1). The groundwater table was detected at 24.6 m depth in borehole S-1 although no groundwater table was observed in S-2 (Fig. 1) during the drilling tasks developed in July 2008. Complementarily, in the two new boreholes drilled in July 2014, the groundwater table was measured at 4.1 and 2.8 m depth in S-1′ and S-2′, respectively. Note that all depth-to-water measurements were made after the completion of the borehole and the stabilization of groundwater levels.

Although groundwater level information is certainly limited, the data recorded during the previous mentioned drilling works, the located springs and the different hydrological properties of the mapped units suggest that the slope presents two different groundwater units: a regional groundwater (GWL_1) input from the north that flows through the most permeable layers (i.e. sandstones) and the fractures of the marly layers, recharging the unit T_1, and a perched groundwater level (GWL_2) which rely on secondary permeability of the unit T_2 and that is subjected to greater local influence.

The chemical analysis performed on water samples taken from S-1 by Saval et al. (2009) showed faecal and total coliform bacteria counts of 8 and 236 colony forming units (c.f.u) per 100 ml and faecal streptococci counts of 2 c.f.u per 100 ml. The origin of these microbiological organisms is attributed to raw sewage from the septic tanks of some old buildings not connected to the sewerage and leaks in the sewer.

The inclinometer installed in geotechnical borehole S-1 (Figs. 1 and 3) shows maximum horizontal displacements in the slope face direction near 15 mm between July 2008 and February 2012 on the more surficial layers (from 0 to 5 m depth). The horizontal displacements

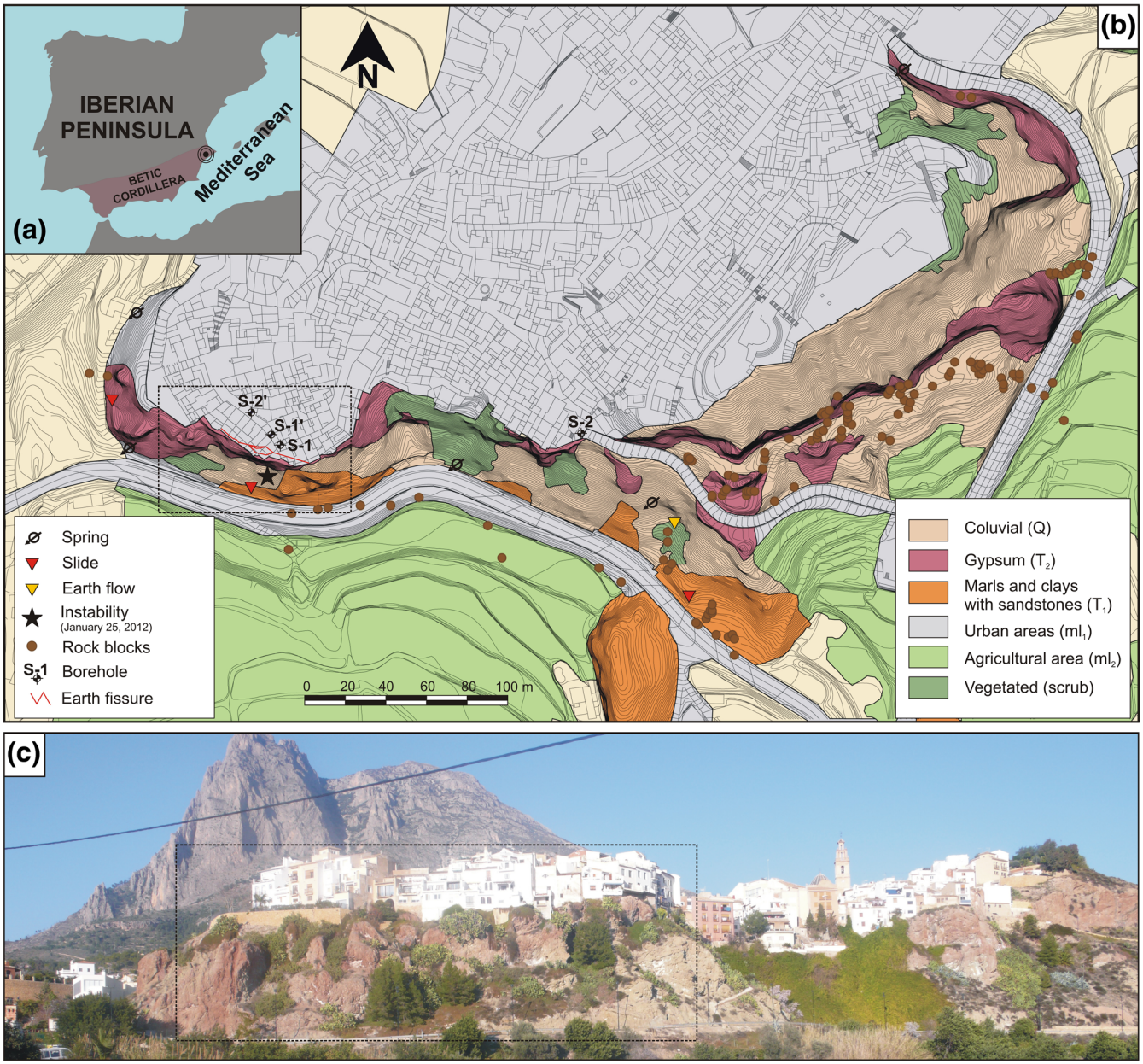

Fig. 1 **a** Location and **b** geology of the study area (modified from Colodrón and Ruíz 1978, Saval et al. 2009). **c** General view of the study area taken in 2011. The *dashed rectangles* plotted in (**b**) and (**c**) correspond to the sector of the slope studied in this work

gradually reduce from 5 up to 21 m depth, being consistent with toppling failure. The available records appear to indicate that the inclinometer is not sufficiently deep to reveal in detail the bottom of the moving region. In the direction parallel to the slope, the displacements are lower than 2 mm and gradually decrease with depth. The independent measurements performed between April 2012 and May 2014 considering a new time origin provided maximum horizontal displacements near 6 and 4 mm in the dip direction and the parallel directions of the slope, respectively.

The aerial orthophotos and 0.5-m resolution digital elevation model (DEM) from Terrasit webpage (GVA 2017) used in this work show that the massive gypsum rocks form a near vertical cliff up to 13 m high in which some long persistent and subvertical fractures and well-defined rock blocks can be recognized. According to the correlation between the S-1 borehole and the outcrop of the gypsum subunit (T_2) on the slope face, the bottom of this layer slightly dips 5–10° towards the south. At the foot of the cliff, the clayey and marly terrains crop out as gentle slopes (i.e. 30–45°) covered by debris deposits and some blocks detached from the upper subunit (T_2). The total height of the slope reaches up to 30 m. The slope was originally densely vegetated at some sectors (Fig. 1) by large trees and heavy cactaceous vegetation (e.g. *Opuntia ficus-indica*). After the January 2012 instability, most of the vegetation was removed by the municipality.

Regarding the stability of the slope, different instability modes have been identified during the field survey in the lower part of the

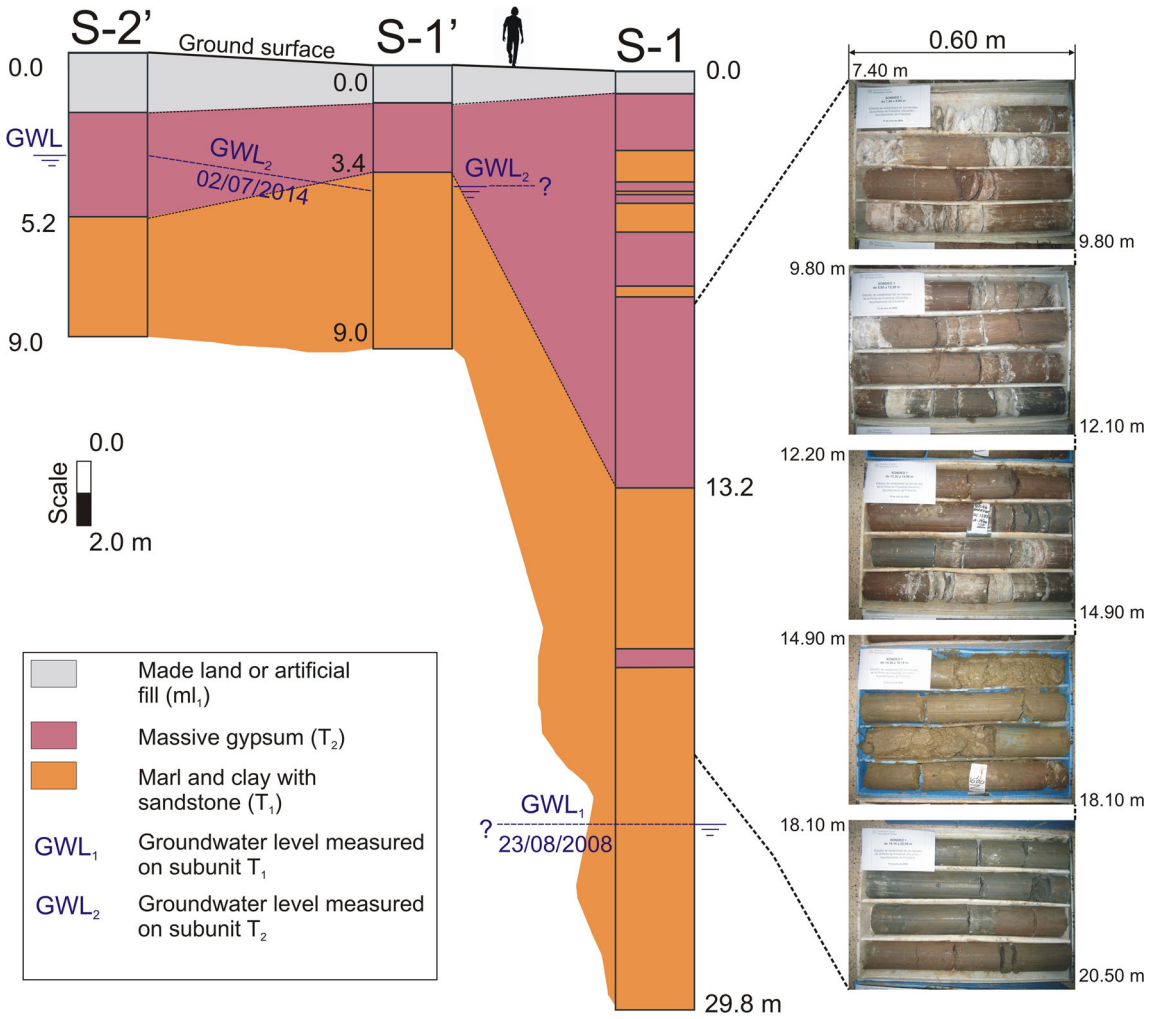

Fig. 2 Geotechnical borehole logs. See the location of the boreholes in Fig. 1

slope: an earth flow, small (<1 m^3) planar slides and numerous rockfalls (according to Cruden and Varnes 1996, Hungr et al. 2014). However, rockfalls are the more common landslide type affecting the upper part of the slope (i.e. T_2 subunit) recognized in the study area. Figure 1 shows the location of the blocks fallen from the main scarps of the slope. The volume of these blocks ranges from 0.1 to 19.0 m^3 and are mainly composed of massive gypsum (Saval, et al. 2009). As a consequence of activity of the slope, a series of corrective measures were taken by the local authorities to improve its security during the second half of 2015. The developed works mainly consisted of the purge of unstable small rock blocks and the construction of an anchored reinforced concrete capping beam under the buildings located on the crown to improve their structural stability. Complementarily, the slope was draped by a cable net combined with a geotextile that was pinned to the slope using rock bolts.

Geophysical surveys

In 2014, 16 ground penetrating radar (GPR) profiles were recorded on the buildings placed on the crown of the slope in order to detect and map subsurface cracks (Ayuntamiento de Finestrat 2014). The multiple lines of data systematically collected were used to map the crack distribution. Additionally, two seismic refraction profiles were made along and across the slope (Ayuntamiento de Finestrat 2014). The methods are described and the profiles provided by the Ayuntamiento de Finestrtat (Ayuntamiento de Finestrat 2014) are analysed in detail in this section.

GPR continuous graphic profiles were recorded using a GSSI SIR-20 data acquisition system coupled to an antenna with a frequency of 200 MHz. The profiles were conducted on 16 linear sections located on the ground floor of the damaged buildings located on the crown of the slope (i.e. on the top of the massive gypsum subunit, T_2) and post-processed to enable the interpretation of the existing features. The depth of the GPR survey covers the upper 6 m of depth as the main aim was to locate the earth fissures affecting the more surficial layers. The results show that the depth of the less stiff materials (i.e. artificial filling, ml_1, and weathered massive gypsum) reaches depths from 1.5 to 5.0 m (Fig. 4). Moreover, the GPR profiles have allowed the recognition of different earth fissures with depths varying from 2 to 4 m. The depth of these cracks reaches maximum values near profile G-6 of 4 m gradually decreasing towards the eastern and western ends.

Table 1 Geotechnical properties of the main geological units of the study area (adapted from Ayuntamiento de Finestrat 2014, Saval et al. 2009)

Properties		Gypsum (T_2)	Marl and clay with sandstone (T_1) Marl and clay	Sandstone
Dry unit weight (kN/m^3)		20.1–22.7	16.4–18.1	–
Moisture content, ω (%)		2.1–8.3	11.5–19.6	–
Particle size	% Gravel	–	8.6–34.4	–
	% Sand	–	10.7–46.1	–
	% Fraction passing no. 200 sieve	–	19.6–76.9	–
Liquid limit, W_L (%)		21.3–36.0	0.0 (non-plastic)–24.2	–
Plasticity index, PI (%)		8.5–14.6	0.0 (non-plastic)–14.5	–
Classification according to Unified Soil Classification System		–	CL-SM	–
Slake durability Id_2 (%)		92.8–98.1	–	90.3
Uniaxial compressive strength, UCS (MPa)		3.5–12.4	0.2–1.1	–
Mean elastic modulus, E_m (N/mm^2)		809.0–4098.9	237.2–255.8	–
Poisson coefficient, υ		0.28–0.45	0.17–1.2	–
Friction angle, φ (°)[a]		26.0–44.7	30.9–32.4	–
Cohesion, c (kN/m^2)[a]		36.0–86.4	0–18	–

[a] Parameter derived from CU direct shear test

Furthermore, the correlation of the different GPR profiles has allowed delineation of the direction of the main earth fissure affecting the buildings that varies from N109E to N130E.

The seismic refraction profiles were conducted along and across the slope (Fig. 4) using a PASI seismograph model 16S-P connected to a linear array of 24 geophones. The type of energy source used consisted of a sledgehammer striking a metal plate. Subsequently, the raw data were interpreted using RAYFRACT software that uses a smooth inversion tomographic method (Intelligent_Resources_Inc 2006). The first seismic refraction profile (P-1) was made on the crown of the slope, on the massive gypsum unit (T_2), on a quasi-horizontal surface, and had a length of 30 m and a depth of penetration up to 3.5 m. The second profile (P-2) was developed downhill from NE to SW along 60 m long reaching a penetration depth over 20 m. This second profile was developed on the marl and clay subunit (T_1).

Profile P-1 (Fig. 4d) shows a low velocity layer (lower than 500 m/s) with a depth up to 1 m corresponding to artificial filling (ml_1). From 1.0 to 2.5–5.0 m depth, there is a layer with velocities varying from 500 to 1000 m/s. This layer corresponds to the more surficial altered gypsum and the more consolidated artificial fillings that in the geotechnical boreholes drilled near the profile reach up to 1.9 m. Below the bottom of the layer of altered gypsum, the velocities increase to over 1000 m/s corresponding to the massive gypsum (T_2) and the marls with sandstone (T_1). Note the existence of a positive relief of massive gypsum in the central part of the profile P-1 that reaches depths up to 0.5 m from ground surface. Profile P-2 (Fig. 4e) shows 0.0–1.0 m of artificial fillings (ml_1) and colluvial sediments (Q) with velocities lower than 500 m/s, a second layer of less stiff marls/clays with 1–5 m thickness and velocities from 500 to 1000 m/s underlaid by stiffer layers of marl, gypsum and sandstone (velocities higher than 1000 m/s). Profile P-2 also confirms the apparent dipping of the contact between the massive gypsum (T_2) and the marl/clay (T_1) subunits towards the south, as deduced from geomorphologic observations.

Remote sensing investigations

Remote monitoring of the slope

Three different ground-based LiDARs (hereinafter terrestrial laser scanners, TLS) were used during a 5-year time-span: (a) an Ilris-3D and a Ilris 3D long range were used for the first and the second field surveys, respectively, and (b) a Leica C10 laser scanner was used for the third and fourth field surveys. Table 2 summarizes the main characteristics of the developed field survey.

For change detection, at least two scans or acquisitions are needed. In this work, the distances between the different point clouds have been carried out using the multi-scale model to model comparison (M3C2) originally developed by Lague et al. (2013).

The main methodological steps are:

1. Step 1. Firstly, the station has been carefully selected in order to have a wide and unimpeded coverage of the slope face (Table 2).
2. Step 2. Once the location was selected, the 3D point clouds (hereinafter referred to as 3DPC) were acquired (Table 2). The first data acquisition (reference points cloud, D_o) was performed on February 2011. Second to fourth scans (comparison points clouds) were performed in August 2012, July 2014 and January 2016, comprising time intervals (temporal baseline) of 553, 1256 and 1822 days, respectively. Regarding the 3DPC acquisition, it is noteworthy that the 2014 3DPC only covers the eastern section of the main slope as this scan was originally performed to study the displacements of the buildings. Thus, no 3D information is available for the western sector of the slope. On the other hand, the 2016 3DPC was acquired once the

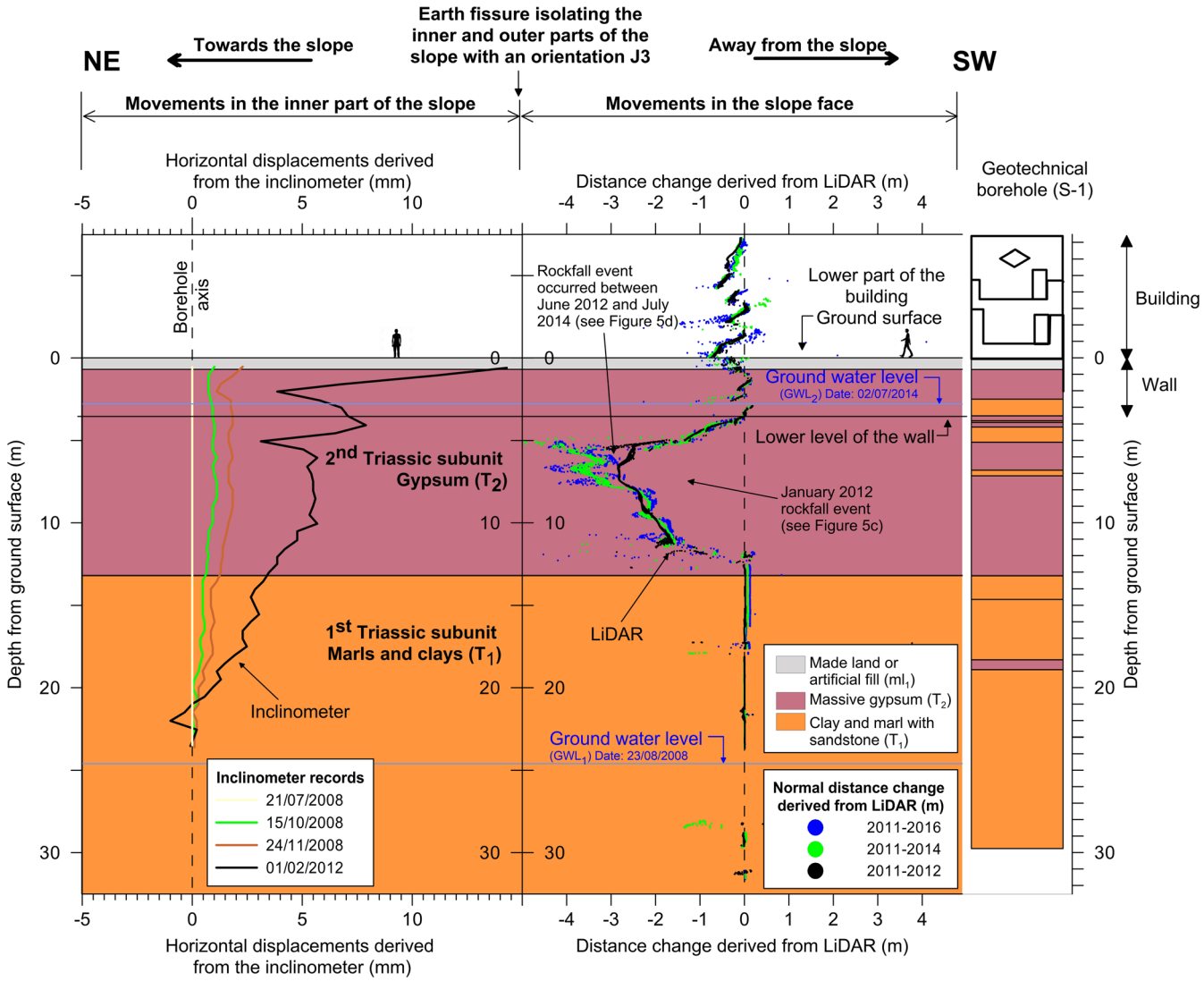

Fig. 3 LiDAR and inclinometer records and S-1 geotechnical borehole log. The section is placed across the building ranked as a Class 6 (partial collapse) in Fig. 10

slope had been draped by the cable net and the geotextile, and thus, the computed changes are affected by the works performed on the slope surface and the installation of the new corrective measures. Therefore, this 3DPC was only used for the study of the building displacements during this period.

3. Step 3. 3D point clouds were aligned, and then, the differences between the reference and the comparison 3DPCs were obtained.

The change detection results derived from the TLS data have been jointly analysed with field data to understand the kinematics of the instability and the associated damage of the houses built-up above the crown of the slope.

Figure 6 shows the large-scale changes (i.e. high magnitude changes represented using a −5 and 5 m colour scale) derived from the processing of 2011–2012, 2012–2014 and 2014–2016 TLS derived 3D point clouds. Note that the negative values of the colour scale indicate loss of material and the positive values material gain. The January 2012 rockfall event that disrupted the road traffic is delineated in Fig. 5c and clearly identified in Fig. 6a. The volume of the detached material has been evaluated at about 60 m^3. The accumulation zone can be also easily recognized as the topography of this area was slightly modified during the conservation works to restore road traffic. Additionally, other minor rockfall events (1.2 to 1.5 in Fig. 6a) can be recognized in the western sector of the affected slope area.

The second processing (i.e. 2012–2014) has allowed the detection of a minor rockfall event (delineated in Fig. 5d and labelled as 2.1 in Fig. 6b) located in the foot of the area previously affected by the January 25, 2012 rockfall, coinciding with the contact between the massive gypsum and the marl and clay subunits (i.e. between subunits T_2 and T_1).

Some corrective measures were taken on the slope in 2016 that substantially modified the comparison point cloud, as mentioned before. Therefore, no changes have been recognized in the third processing (i.e. 2014–2016).

The changes not labelled in Fig. 6 are associated with outliers that generate isolated changes, man-made modifications (e.g. the anchored reinforced concrete capping beam built between 2014

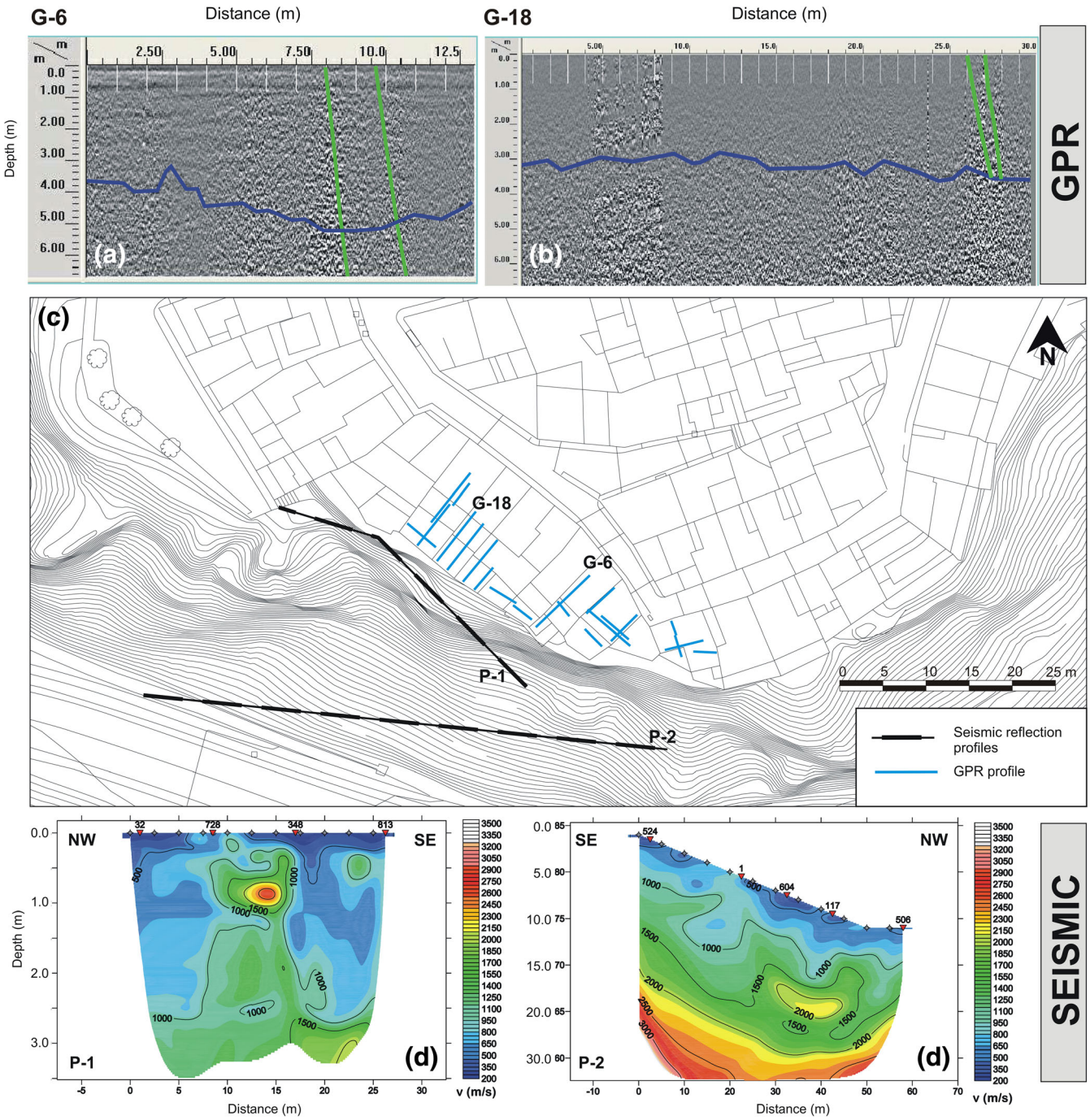

Fig. 4 **a**, **b** G-6 and G-18 ground penetrating radar profiles. *Blue lines* represent the top of the massive gypsum subunit (T2) and *green lines* the earth fissures. **c** Location of the ground penetrating radar and seismic refraction profiles. Note that although the figure represents the 16 GPR transects performed, only profiles G-6 and G-18 are shown as examples. **d**, **e** Seismic refraction profiles made on and along the slope. Notice that the *vertical* and *horizontal scales* of P-1 and P-2 profiles are different in both plots

and 2016 on the top of the slope; Fig. 6c) and vegetation phenology (mainly affecting the results shown in Fig. 6a, b, due to the strong clearing and pruning works performed during these periods).

The results have been also represented using a more detailed scale (i.e. using a − 0.3 to 0.3 m colour scale) to evaluate the small-scale changes due to the displacements of the buildings. These data have allowed measurement of centimetre scale changes in some parts of the buildings located upon the slope (Fig. 7). These changes are higher in the second and third analysed period reaching up to 12 cm (Fig. 7c).

Identification of discontinuities from 3DPC

The 3DPCs obtained during the 2011 and 2012 surveys have been also used for the remote characterization of rock mass discontinuities using the discontinuity set extractor (DSE) open-source software developed by Riquelme et al. (2014). This software

Table 2 Summary of the TLS field surveys

Parameters	2011 February	2012 August	2014 July	2016 January
Relative time span (days)	0	553	1256	1822
LiDAR model	Ilris 3D	Ilris 3D (long range)	Leica C10	Leica C10
Mean distance of scanning (m)	276	276	120	133
Acquisition velocity (points/s)	2500	10,000	50,000	50,000

identifies and defines the different planar discontinuities of the rock mass slope surface by applying an analysis based on a neighbouring points coplanarity test, finding principal orientations by the non-parametric technique Kernel Density Estimation (Botev et al. 2010) and identifying clusters by the density-based scan algorithm with noise (Ester et al. 1996). This information has allowed the identification of the most important discontinuity sets affecting the slope from the available 3DPC corresponding to 2011 (i.e. before the largest failure) and 2012 (i.e. after the large failure). The results are shown in Figs. 8 and 9 in which three and two discontinuity sets have been recognized from the 2011 and 2012 3DPCs, respectively, in the gypsiferous massif (i.e. subunit T_1). The three discontinuities identified from 2011 3DPC present the following orientations: 336/62 for J1 (blue in Fig. 8e), 162/68 for J2 (red in Fig. 8e) and 18/79 for J3 (green in Fig. 8e). The processing of 2012 data only allows recognizing two sets of planar discontinuities: 337/66 for J1 (blue in Fig. 8f) and 170/49 for J2 (red in Fig. 8f).

Figure 9b represents the stereographic projection of the different discontinuity sets derived from the analysed 3DPCs (J1, J2 and J3) as well as the zone of the great circles representing the variability of the slope (S) direction. The zone representing the range of directions of the earth fissure recognized by means of the GPR technique is also represented in the plot. From the figure, it is clear that J1 (the most exposed discontinuity) and J3 present a similar subvertical dip value and dip into the slope being geometrically compatible with a toppling failure mode. On the other hand, discontinuity set J2 dips out of the slope with a variable dip between 49 and 68° being prone to planar failure. It is noteworthy that the orientation of J3 obtained using LiDAR 3DPC is very similar to that derived from GPR results for the main earth fissure affecting the buildings (Fig. 8b).

Forensic analysis of buildings

The buildings located on the top of the slope present important damage mainly consisting of cracks and fissures that were documented, described and mapped during fieldwork. Furthermore, some of the buildings placed on the crown of the slope present tilting since their load-bearing walls are partially founded on the most active rock block and partially founded on the inner less active rock block. The differential vertical displacements between both rock blocks cause the tilt of the building.

Complementarily, the damage of the buildings was ranked according to Cooper's (2008) building damage recording scheme, based on distribution and severity of the damage. The building structures of these properties are mainly composed of load-bearing masonry walls and wood joists, which are quite sensitive to vertical and horizontal differential displacements due to their rigidity (Burland and Wroth 1975).

Field works have allowed the recognition of important structural damage (class 3 to class 6) on buildings, mainly concentrated near the slope face, decreasing as we move away from the cliff. In fact, most of the damaged buildings do not exhibit any damage or lesser damage on the north façades, as the severe damage is mainly concentrated on the portion of the buildings founded on the main unstable rock block (Figs. 7d and 10). Furthermore, some minor damage (class 1 to class 2 in Fig. 10) have been observed as incipient fissures on the façades of some buildings, as well as on the rigid pavement of the street.

Interpretation and synthesis

The integration of the available geomorphological, structural, geotechnical, forensic and geophysical information as well as the monitoring data provided by the TLS and the installed inclinometer provided very relevant information for the understanding of the studied instability and its kinematics.

The slope has historically exhibited some slope instabilities, including the recent occurrence of the 60 m^3 event that happened during January 2012 and a minor rockfall event occurred between June 2013 and July 2014 (Figs. 1 and 5). Coetaneously, some buildings founded near the cliff were severely damaged due to a slow-moving lateral spreading, causing considerable social alarm in the local population. The lithological, structural and geomorphological information acquired in this study suggests that there is an important structural and lithological control of the observed instabilities. Indeed, the co-existence of Triassic weak and brittle massive gypsum (T_2) laying over less competent lithologies (i.e. marls and clays from T_1 subunit) (Fig. 11) controls the generation of slope instabilities. This type of landslide typically develops on slopes formed by a soft and ductile material capped by a fragile rock mass (e.g.Elorza and Gutiérrez Santolalla 1998, Gutiérrez-Santolalla et al. 2012, Gutiérrez et al. 2012, Mantovani, et al. 2013). Additionally, the delimitation of the massive gypsum blocks by subvertical crack J3 that presents an orientation 18/79, parallel to the free face of the slope (Fig. 9), facilitates the mobilization of portions of massive evaporitic rock over the less competent lithologies, following an undefined basal shear surface. Similar behaviour has been pointed out in analogous study areas before (Gutiérrez, et al. 2012, Mantovani, et al. 2013, Pasuto and Soldati 2013). Therefore, the geomorphological, lithological and structural evidences point to the existence of a rock spreading landslide, which has been amplified by the loss of lateral support due to recent rockfall occurrence.

As previously mentioned, inclinometer S-1, which is 7 m from the slope face (Fig. 1), showed maximum horizontal internal displacements on the more surficial layers of the slope, gradually reducing with depth (Fig. 3). On the other hand, the TLS data

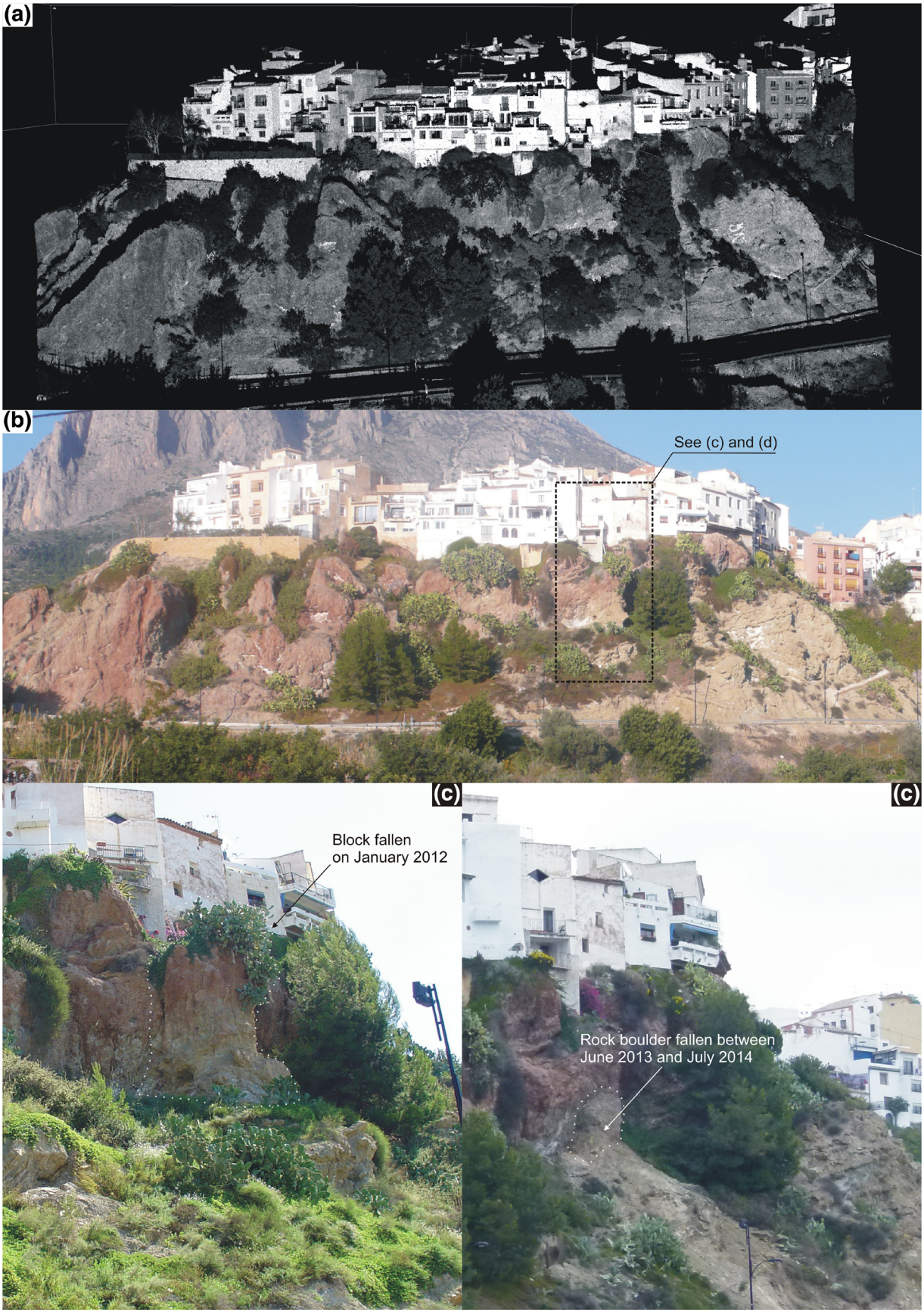

Fig. 5 **a** 3D point cloud acquired in the February 2011 LiDAR survey. **b** General view of the scanned area (February 2011). **c** Rock blocks destabilized in January 2012 and **d** during the period 2013–2014

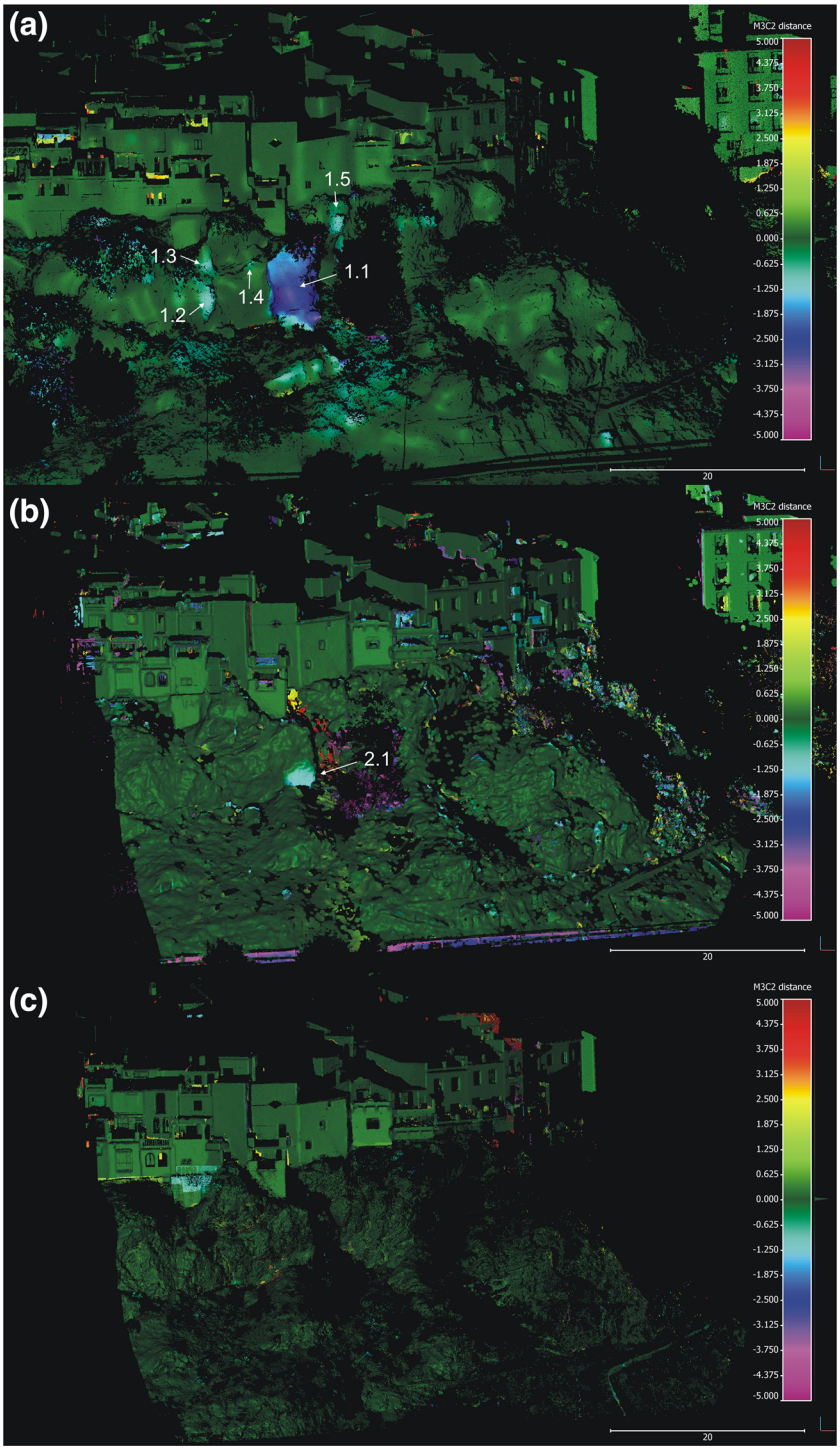

Fig. 6 Comparison of LiDAR models showing large-scale changes corresponding to **a** February 2011 vs. August 2012, **b** August 2012 vs. July 2014 and **c** July 2014 vs. January 2016. The labels indicate the rockfall events detected for each period. Note that the two last images only cover the easternmost sector of the slope since the 2014 3DPC was only acquired for the study of the buildings placed on this sector

analysis provided the changes produced on the slope face between 2011 and 2014 (Fig. 3). Note that, as previously described, in 2016, a protection net was installed and then the TLS data of this date are not valid for the study of the slope face kinematics. Assuming that these changes correspond to the actual downhill displacements, we can note that the maximum values measured by TLS for the periods 2011–2012 and 2011–2014 are near 15 cm, being slightly higher in the upper part of the slope and the lower part of the buildings (Figs. 3, 6 and 7). Notice that, as the inclinometer S-1 is placed on the back of the rock block delimited by the main earth fissure (Figs. 1 and 3), its displacements are lower than those measured by means of TLS data on the slope face and the

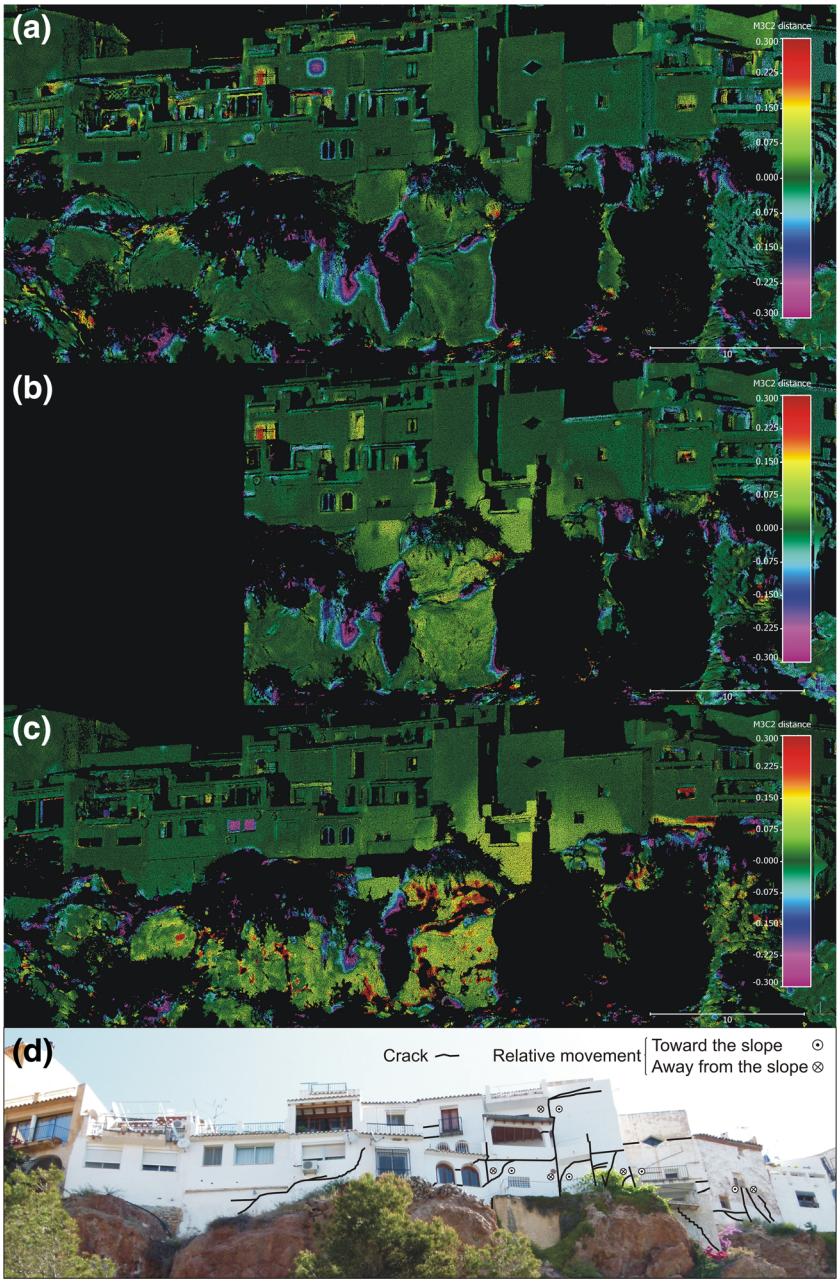

Fig. 7 Comparison of LiDAR models showing small-scale changes corresponding to **a** February 2011 vs. August 2012, **b** February 2011vs. July 2014 and **c** February 2011 vs. January 2016. Note that the colour scale has been adjusted to small magnitude changes. **d** Observed cracks in the façades of the buildings placed on the slope and *symbols* indicative of the relative sense of motion

buildings as expected. According to these data, the maximum velocity of the main mobilized gypsiferous rock mass is 20 mm/year. Similarly, the maximum velocities of the back block, in which the inclinometer was installed (Fig. 11), for the 2008–2012 and the 2012–2014 periods is 4.2 and 2.9 mm/yr., respectively. Therefore, two different kinematic characteristics can be distinguished associated with the rock mass blocks delimited by the main earth fissure that belongs to discontinuity set J3 (Fig. 11): (a) a very slow movement (according to Cruden and Varnes 1996) affecting the outermost part of the slope corresponding to the front of the rock spreading and (b) extremely slow (according to Cruden and Varnes 1996) displacements associated to the innermost part of the rock spreading.

The developed forensic analysis agrees the previous results, showing that there is a clear zonation of the damage affecting the buildings (Figs. 7d and 10). The further away from the slope, the lower the damage, since most of the cracks affecting the buildings are concentrated near the slope face. In fact, some of the most damaged buildings located on the front of the slope crown even show very slight damage on their north façade. The explanation for this is that some buildings are partially founded on the unstable massive gypsiferous rock blocks (delimited by the

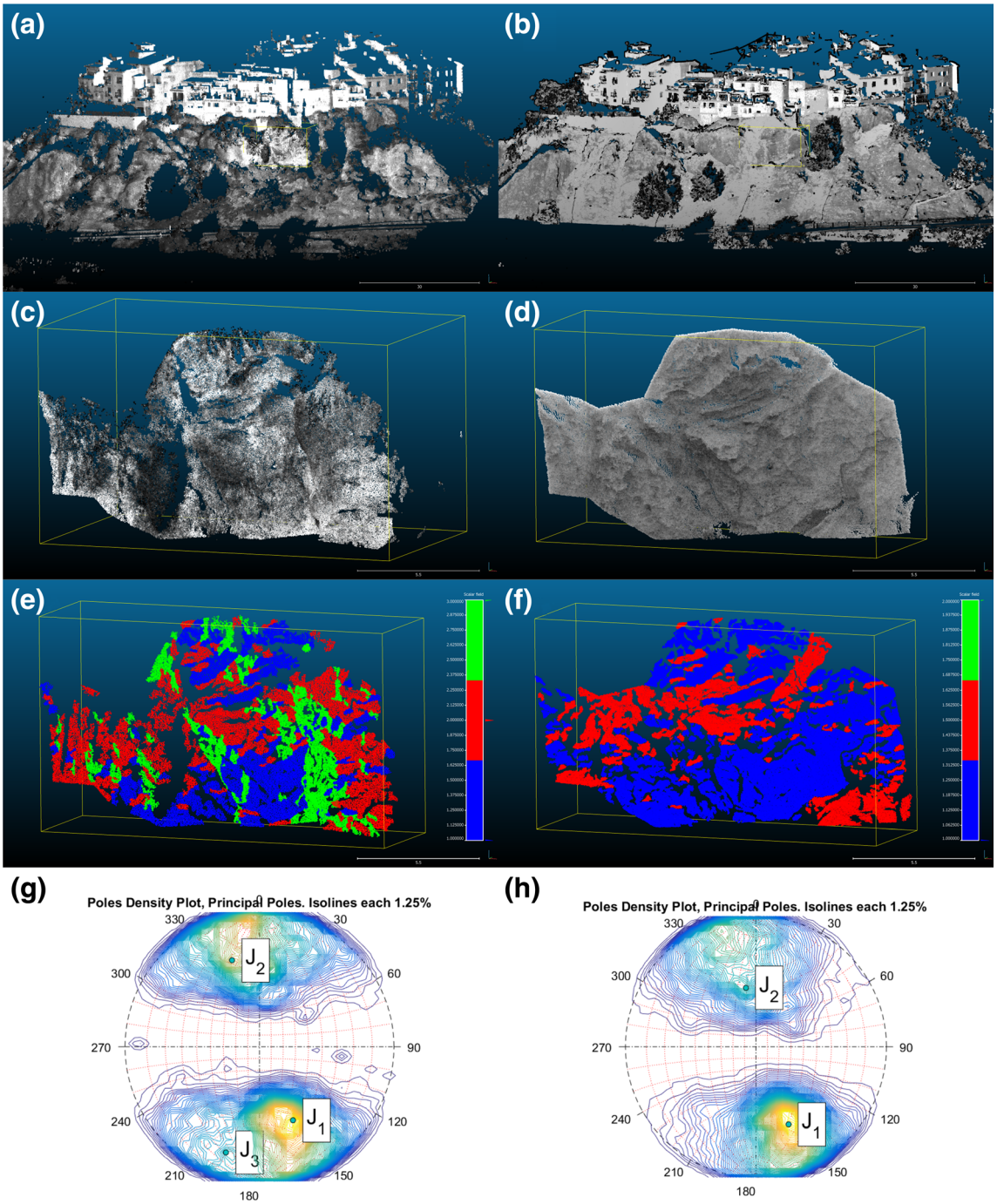

Fig. 8 3DPCs obtained from **a** 2011 and **b** 2012 surveys for the whole slope. **c**, **d** Correspond to the 2011 and 2012 3DPCs, respectively, of the processed areas located on the failure sector. **e**, **f** Show the identification of the discontinuity sets derived from the 2011 and 2012 LiDAR surveys. Note that each *colour* correspond to a different discontinuity set. **g**, **h** The normal vector density plot for 2011 and 2012 3DPC, respectively. See a picture with the location of the discontinuity sets on Fig. 9a

recognized earth fissure) and the other part of the building is placed on a metastable block with a lower activity (Fig. 11).

TLS information (Fig. 7) also agrees the distribution of the observed damage. The TLS-derived displacement plot shows maximum displacement values up to 15 cm on the line of sight between February 2012 and January 2016 concentrated on the lower balcony of the buildings classified as "Partial collapse" in agreement with the forensic analysis (Fig. 10). These displacements gradually reduce towards the east, the west and from bottom to top of the buildings and perfectly match the area defined by the cracks mapped on the building façades (Fig. 10). Additionally, the typical distribution of cracks (Fig. 7) of the south façades of the buildings (i.e. dipping towards east and west on both extremes, respectively) indicates that the central part of

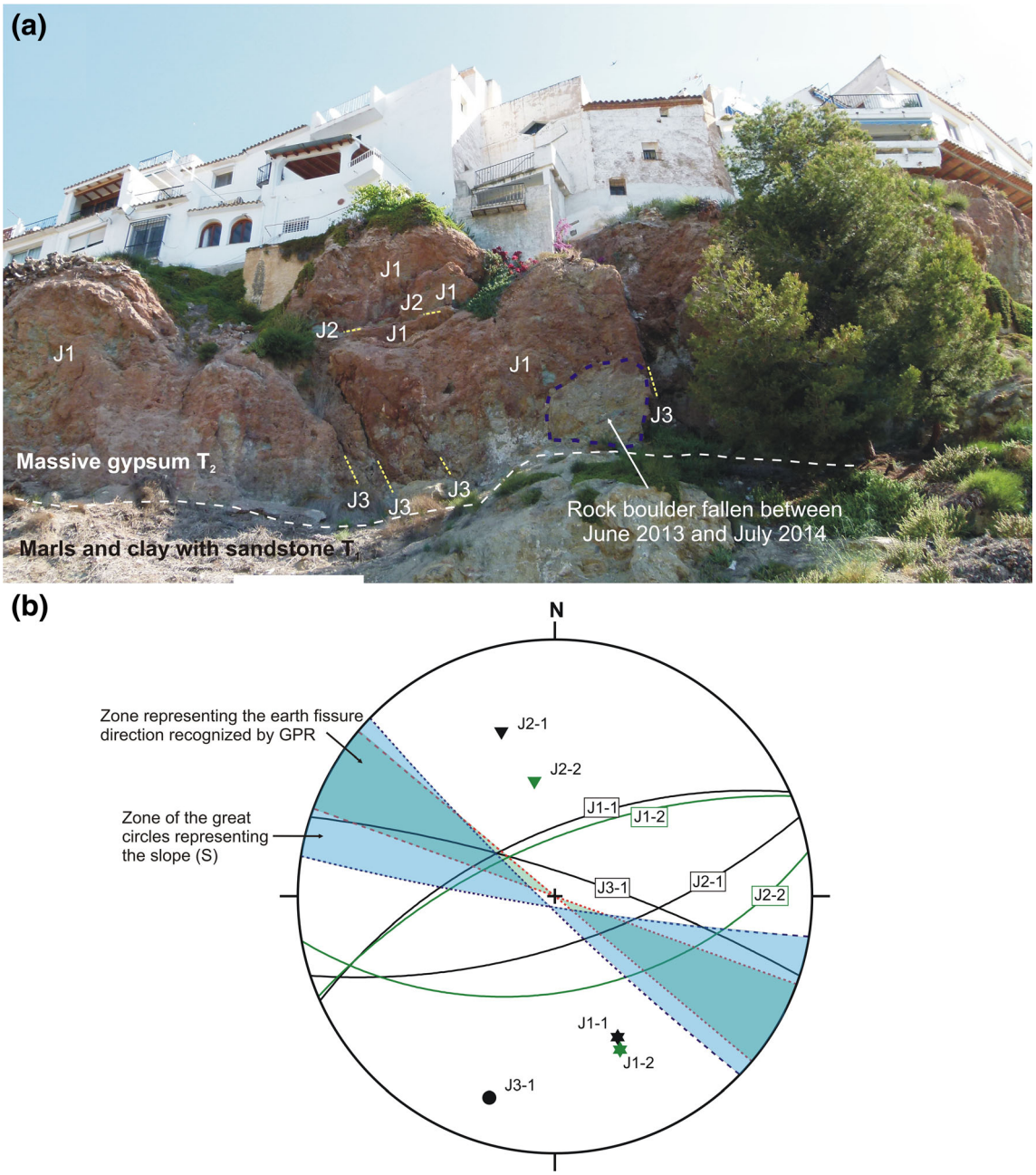

Fig. 9 **a** Location of the discontinuity sets J1, J2 and J3 affecting unit T2 semi-automatically derived from LiDAR 3DPCs. *Dashed line* maps the contact between the massive gypsum (T2) and the marl and clay (T1) subunits and *dotted line* delineates the rock block fallen between June 2013 and July 2014. Pictures were taken on June 2013. **b** Stereoplot representing the poles and great circles of the discontinuities derived from the 3DPC and the zones of the great circles representing the earth fissure recognized by GPR and the slope. *Black* (J1–1, J2–1 and J3–1) and *green* (J1–2 and J2–2) poles were derived from the 2011 and 2012 scans, respectively

the area has been affected by sagging accompanied by the horizontal displacements measured by TLS and the inclinometer and observed in Fig. 6d.

The small vertical component of the displacement is also perceived in some cracks recognized on the floor of the damaged buildings that exhibit a small vertical throw (d_v). This circumstance indicates that the lateral extension of the clay and marl subunit is accompanied by small subsidence and tilt of the overlying massive gypsiferous rocks as other researchers have described (e.g. Radbruch-Hall 1978, Schultz-Ela 2001).

Groundwater existing on the slope could play a key role on the kinematics of this phenomenon due both to chemical and physical components. As previously explained, the groundwater present on subunit T_1 seems to have a regional input. However, the perched groundwater of subunit T_2 presents a greater local influence of the surface runoff that is directly poured over the slope and the discharge from septic tanks and the sewers. This water can infiltrate through the discontinuities of the gypsiferous massif (subunit T_2) to the lower impervious layers of clay (subunit T_1) partially filling the existing tension cracks.

Fig. 10 Damage observed in the buildings placed in the crown of the studied slope. Note that the level of damage of the buildings has been ranked according to Cooper's (2008) classification. The main damage observed on the buildings placed on the top of the slope consists of **a** long persistence and wide-aperture cracks (Fig. 10a–g) affecting the walls and the floor of the buildings, **b** 45° cracks on the lateral walls of the buildings dipping away from the slope, **c** longitudinal displacements of the wood joists towards the slope (Fig. 10e, f) and **d** relative displacement (tilt) of the north façade towards the slope face (Fig. 10e)

The groundwater that flows through the gypsum-clay/marl contact can dissolve the bottom of the gypsum blocks up to saturation, eroding and causing a gradual loss of strength that can contribute to the observed subsidence as described by Gutiérrez-Santolalla et al. (2012). Complementarily, this groundwater can saturate the underlying clay and marls modifying its consistence state and enabling their deformation and the consequent subsidence of the overlaying gypsum rock mass as previously described. Groundwater can also cause other well-known unfavourable effects on the stability of the slope as hydrostatic pressure and internal erosion.

In addition, the loads transmitted by the structures built-up to the edge of the cliff may control the lateral spreading due to their negative influence on its stability. Additionally, the slope was vegetated by some large trees and heavy cactaceous plants (Figs. 1 and 5b, c) before remedial actions were taken. This vegetation could exert a positive influence mainly on the slope stability of the marls and clays of T_1 subunit due to the removal of groundwater and the increase of soil

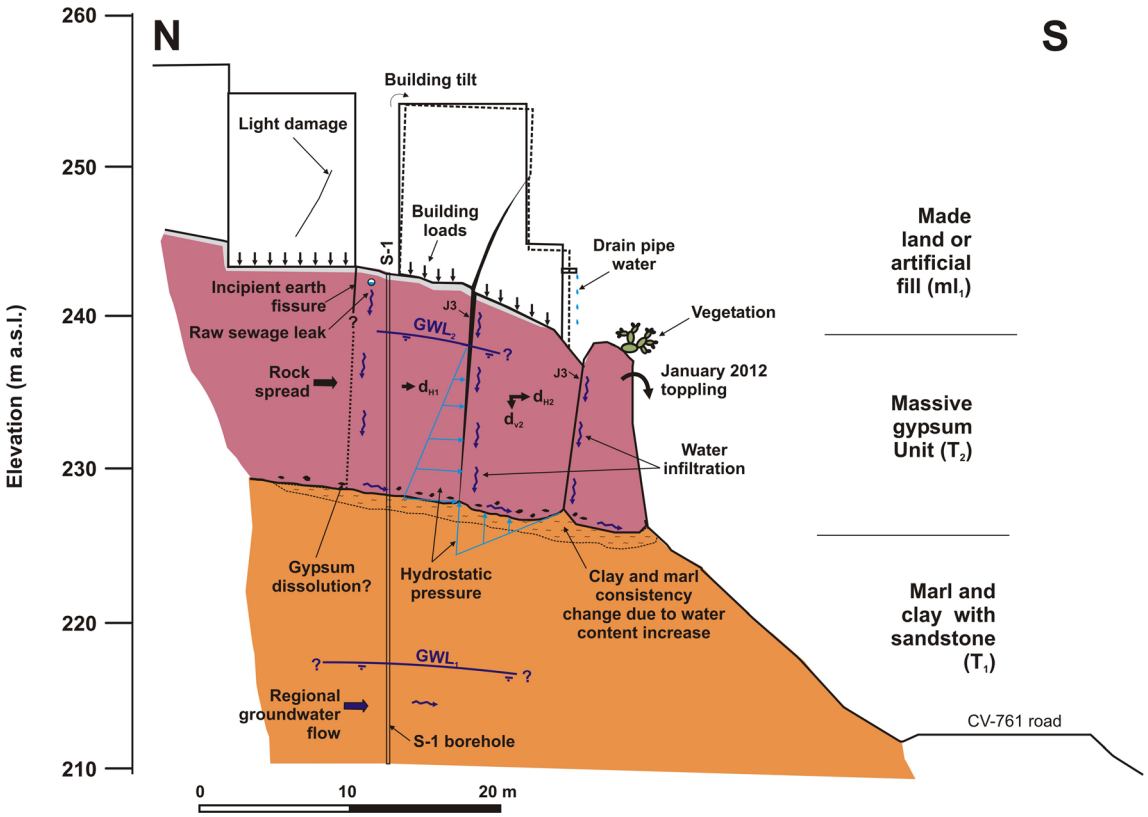

Fig. 11 N-S cross-section of the studied slope based on the information provided by the different techniques. GWL_2: groundwater level on subunit T_2; GWL_1: groundwater level on subunit T_1; d_{H1}, d_{H2} and d_{v2} are the horizontal and vertical displacements of the rock blocks, being $d_{v2} < d_{H1} < d_{H2}$

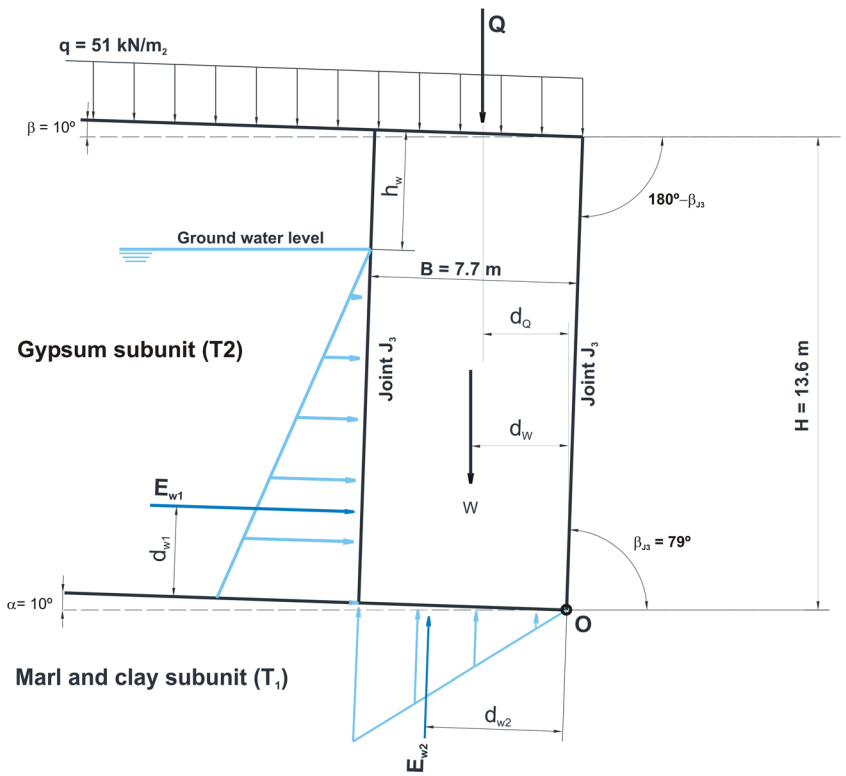

Fig. 12 Geometry and forces considered for the stability analysis of the rock slope

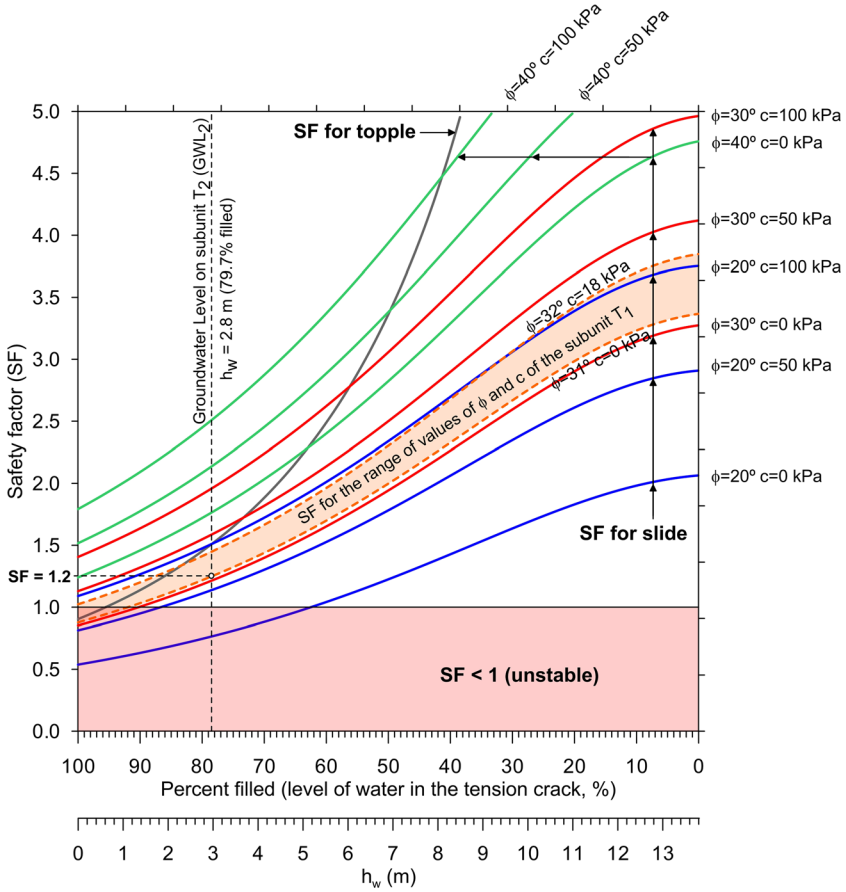

Fig. 13 Summary of the values of the safety factors of the slope obtained from the performed sensitivity analysis considering toppling and planar failure modes

shear strength by roots. However, according to the observed land sliding mechanism, the vegetation growing on the massive gypsum (T_2) increased the vertical loads due to its own weight as well as the horizontal loads and the bending moments induced by the wind. Furthermore, the roots could act as wedges, contributing to the fracturing of the gypsiferous rock mass.

The 60 m^3 instability that occurred on this slope in January 2012 was classified as a toppling according to the morphology of the original block and the observable rupture scar (i.e. J1 discontinuity set) after the failure (Figs. 5c and 9a). This main failure was accompanied by some minor rockfall instabilities of nearby rock blocks (Fig. 6a). The second registered instability occurred between June 2013 and July 2014 and also consisted of a toppling of a metastable rock block controlled by the set J1 (Figs. 5d and 6b). Neither an earthquake nor rainfall was recognized in the previous days to these events, and therefore, the trigger of these events is attributed to the natural dynamics of the rock spreading. Actually, it is well known that despite the low displacement rate of rock spreadings, they can induce hazardous, collateral, faster landslides as topples and rockfalls, mainly on edges of the mobilized rock mass that are not confined laterally (Delgado et al. 2011, Gutiérrez, et al. 2012, Mantovani, et al. 2013). Additionally, some authors suggest that rockfalls can potentially be considered as precursory behaviour prior to a larger slope failure or landslide (e.g. Rosser et al. 2007, Royán, et al. 2014). In this case of study, it can be seen that the gypsiferous rock block destabilized during the January 2012 event was located in the depth range in which maximum horizontal displacements up to 8 mm were measured between July 2008 and February 2012 by means of the inclinometer (Fig. 3). Furthermore, this sector of the slope presents the maximum small-scale displacements (near 20 cm) derived from LiDAR between 2011 and 2014 (Fig. 6). Therefore, it seems that the recorded rockfalls are exacerbated by the larger failure observed by the inclinometer and the LiDAR.

Figure 11 shows an interpretative cross-section of the rock spread summarizing the different integrated aspects considered in this work, the kinematics, the mechanisms and the conditioning factors as previously described.

Finally, a simple two-dimensional limit equilibrium analysis of the slope has been performed to evaluate the possibility of planar sliding and toppling failure. The translational slip model assumes that the block slides along the contact between subunits T_1 and T_2, as shown in Fig. 12, and the safety factor (SF) is calculated as:

$$SF = \frac{C \times A + [(W + Q)\cos(\alpha) - E_{W2}]tg(\phi)}{(W + Q)\sin(\alpha) + E_{W1}} \quad (1)$$

where c and ϕ are the cohesion and the friction angle, respectively, along the area of contact A between the subunits T_1 and T_2 that dips $\alpha = 10°$ away from the slope, W is the weight of the wedge, Q is

the resulting load due to the buildings (calculated from a distributed load of 51 kN/m^2 corresponding to a two-floor masonry building with wood joists and concrete floor slabs) and E_{W1} and E_{W2} are the hydrostatic forces acting on the tension crack and the sliding surface, respectively.

Toppling model considers that the rock block turns around its base (O in Fig. 12) and the SF is calculated as

$$SF = \frac{d_W \times W + d_Q \times Q}{d_{W1} \times E_{W1} + d_{W2} \times E_{W2}} \quad (2)$$

where d_W, d_{W1}, d_{W2} and d_Q are the perpendicular distances between the points at which the forces are applied and the axis of turning (O in Fig. 12).

Note that both models consider that the rock block is vertically delimited by the joint set J3 that corresponds to the tension crack recognized in the geophysical and forensic analysis and identified from 3DPC.

Since in this case of study geotechnical properties pose some uncertainties in the simulation, each significant parameter (i.e. the friction angle, the cohesion and the percent filled of the tension crack) has been varied systematically over its maximum credible range in order to determine its influence upon the factor of safety. The other parameters have remained constant. The results of the analysis are shown in Fig. 13.

The plot shows that the SF for toppling increases very quick when groundwater level falls and, as it is well known, does not depend on the shear strength on the sliding plane. Furthermore, SF only reaches values lower than 1 when more than 95% of the tension crack is filled with groundwater (i.e. when h_w is lower than 0.6 m).

For planar sliding, SF considerably increases with the friction angle and the cohesion, although the groundwater level exerts a greater influence. Assuming that the sliding of the block occurs along a failure surface involving the subunit T_1 and considering the upper and lower bound values of friction angle (ϕ from 31 to 32°) and cohesion (c from 0 to 18 kPa) (Table 1), we can calculate the envelope of the SF (plotted in light orange in Fig. 13). These values show that SF is less than 1 for h_w lengths lower than 1.1 m (i.e. more than 92% of the crack filled). Thus, the results indicate that when the perched groundwater level (GWL_2) increases, both the toppling and the sliding SF reduce. However, SF reaches values lower than 1 (unstable) firstly for planar sliding before doing so for toppling failure. Additionally, for h_w values up to 2.8 m (79.7% of the crack filled; Fig. 13), as the one recorded in borehole S-2′, the safety factor is 1.2 for planar failure and 1.4 for topple. When the groundwater level falls under the contact between subunits T_1 and T_2, SF becomes infinity for toppling and 3.4 for planar sliding. Therefore, the stability analysis supports the sliding of rock blocks caused by ground water pressure as the main instability mechanism, although when high percentages of the tension crack are filled by groundwater (more than 95%), the blocks can also be affected by both toppling and sliding processes.

Conclusions

The interpretation of this rock spreading has been performed using data collected from the ground surface, the subsurface and buildings placed on the slope. Table 3 summarizes the different

Table 3 Type of data sources and investigation techniques used in this work for the investigation of the landslide (adapted from Travelletti and Malet 2012)

		Geological mapping	DEM, orthophotos and oblique photographs	Boreholes logs	Laboratory tests	Inclinometer	GPR	Seismic refraction	Remote Sensing - monitoring	Remote sensing - structural	Forensic analysis
Data type	Kinematic					√			√		√
	Geomorphologic	√	√							√	
	Geological	√		√			√	√		√	
	Geotechnical			√	√						
	Petro-physical			√	√		√	√			
	Spatial extension	2D	2D	1D	3D	1D	2D	2D	3D	3D	2D
Type of information		Surface	Surface	Internal	Internal	Internal	Internal	Internal	Surface	Surface	Surface
Resolution		m	m	cm	cm	mm	dm	dm	mm	mm	m

Internal: Information on the internal layer geometry and properties. Surface: information on the landslide boundary at the ground surface

investigation techniques used in this work and the provided type of data, their spatial extension and the contribution to surficial (at the ground surface) or internal (on the internal layer geometry and properties) information. Inclinometer and TLS-derived information provided quantitative 3D information about the inner and the surficial kinematics, respectively, of the landslide. Complementarily, forensic information has allowed delimiting the extension of the landslide, the parts of the rock spreading exhibiting higher accumulated displacements, the small vertical component of the movement and even the type of movement. The characteristic geomorphology of the steep slope defined by the massive gypsum subunit has contributed to the definition of the landslide slip surface through the geological mapping and the use of cartographic resources (i.e. aerial photographs and a DEM). Furthermore, the structural mapping of the discontinuities using the 3DPCs derived from TLS have provided useful geomorphologic information for the definition of the failure surfaces controlling the instability that occurred in January 2012 (i.e. J1 discontinuity set), the orientation of the discontinuity set J3, to which belongs the main earth fissure detected by GPR, as well as other potential sliding planes. Geophysical profiles contributed to the definition of the geometry of the different lithological units and the location of the earth fissures controlling the rock spreading. Geological mapping and borehole logs provided surficial and internal information, respectively, of the geological units involved on this landslide. The geological descriptions were supported by the geotechnical information provided from the recovered soil and rock cores from the boreholes. The results of the geotechnical tests contributed to the differentiation of the geomechanical properties of the units affected by the landslide. Petro-physical properties of the sub-surface obtained from 2D geophysical tests and 1D geotechnical boreholes were used to determine the extent of the different units and to define the geological contacts and the earth fissures delimiting the rock blocks. Finally, the limit equilibrium analysis of the rock block performed considering toppling and sliding failure mechanisms supports the sliding of the rock blocks that can be also accompanied by toppling when groundwater level is very high. The impact of groundwater levels on the stability of the slope is also very clear.

The comprehensive analysis of the different data from this multi-technique and multidisciplinary approach suggests the vertical fracturing of the gypsum massif (T_2 subunit) by the discontinuity sets J1 and J3 into different independent rock blocks. These bodies slide over the ductile and less competent marls (T_1 subunit) exhibiting a Very slow to Extremely slow velocity according to Cruden and Varnes' classification (1996) that affects the buildings placed on the slope. This general movement induces faster landslides on the unconfined edges of the rock mass as shown by the joint analysis of inclinometer and LiDAR monitoring data. Forensic analysis confirms the assumptions of the occurrence of small vertical displacements of the massive gypsum blocks through the shape, distribution and aperture of the mapped cracks.

As a conclusion, the integration of geomorphological, structural, geotechnical, monitoring, geophysical, forensic information of this urbanized gypsiferous slope and simple limit equilibrium models has proved to be effective for an integral understanding of a complex rock spreading landslide as well as its kinematics, activity and conditioning factors. Furthermore, the continuation of the investigation will allow us to know whether the corrective adopted measures are effective or, on the contrary, new stabilization actions will be required.

Acknowledgements

Authors acknowledge the Excelentísimo Ayuntamiento de Finestrat for the provided geotechnical, geophysical and graphical information and the authorization for publishing the available data and INGYOB S.L for the provided photos. F. Gutierrez (UNIZAR) kindly provided useful scientific literature. This work has been supported by the University of Alicante under the project GRE14-04, Generalitat Valenciana under the project GV/2011/044, by the Ministry of Education, Culture and Sport trough the project PRX14/00100, by the Spanish Ministry of Economy and Competitiveness and EU FEDER funds under project TIN2014-55413-C2-2-P, by Swiss National Science Foundation (project numbers 138015 and 144040) and by the European Commission project MOMIT (Ref. no 777630). The second author would like to acknowledge the support received from the H2020 Program of the European Commission under the Marie Skłodowska-Curie Individual Fellowships (MSCA-IF-2015-705215).

References

Alexander D (1986) Landslide damage to buildings. Environ Geol Water Sci 8:147–151. doi:10.1007/BF02509902

Ausilio E, Zimmaro P (2016) Landslide characterization using a multidisciplinary approach. Measurement. doi:10.1016/j.measurement.2016.01.009

Ayuntamiento de Finestrat (2014) Estudio geotécnico del proyecto de estabilización de talud y viviendas en la calle fondo n° 21–37 finestrat—alicante. Ayuntamiento de Finestrat, pp 141

Botev ZI, Grotowski JF, Kroese DP (2010) Kernel density estimation via diffusion. Ann Stat 38:2916–2957

Burland JB and Wroth CP (1975) Settlement of buildings and associated damage

Climate-Data (2016) Climate data

Colodrón I and Ruíz V (1978) Mapa geológico de españa, hoja 847, villajoyosa. In: España IGd (ed) MAGNA, Instituto Geológico de España, Madrid

Cooper AH (2008) The classification, recording, databasing and use of information about building damage caused by subsidence and landslides. Q J Eng Geol Hydrogeol 41:409–424. doi:10.1144/1470-9236/07-223

Crosta GB, di Prisco C, Frattini P, Frigerio G, Castellanza R, Agliardi F (2014) Chasing a complete understanding of the triggering mechanisms of a large rapidly evolving rockslide. Landslides 11:747–764. doi:10.1007/s10346-013-0433-1

Cruden DM, Varnes DJ (1996) Landslide types and processes. In: Turner AK, Schuster RL (eds) Landslides: Investigation and mitigation (special report). National Research Council, Transportation and Research Board Special Report, Washington, DC, pp 36–75

Delgado J, Vicente F, García-Tortosa F, Alfaro P, Estévez A, Lopez-Sanchez JM, Tomás R, Mallorquí JJ (2011) A deep seated compound rotational rock slide and rock spread in se spain: structural control and dinsar monitoring. Geomorphology 129:252–262

Elorza MG, Gutiérrez Santolalla F (1998) Geomorphology of the tertiary gypsum formations in the ebro depression (Spain). Geoderma 87:1–29. doi:10.1016/S0016-7061(98)00065-2

Ester M, Kriegel H-P, Sander J and Xu X (1996) A density-based algorithm for discovering clusters in large spatial databases with noise KDD 96: 226–231

Ferrero A, Migliazza M, Roncella R, Rabbi E (2011) Rock slopes risk assessment based on advanced geostructural survey techniques. Landslides 8:221–231. doi:10.1007/s10346-010-0246-4

Franklin JA, Chandra R (1972) The slake-durability test. Int J Rock Mech Min Sci Geomech Abstr 9:325–328. doi:10.1016/0148-9062(72)90001-0

Gorsevski P, Brown MK, Panter K, Onasch C, Simic A and Snyder J (2015) Landslide detection and susceptibility mapping using lidar and an artificial neural network

approach: a case study in the cuyahoga valley national park, ohio. Landslides: 1–18. doi: 10.1007/s10346-015-0587-0
Gutiérrez-Santolalla F, Arauzo T, Desir G (2012) Deslizamientos en el escarpe en yesos de alfajarín (zaragoza). Cuat Geomorfol 8:12
Gutiérrez F, Linares R, Roqué C, Zarroca M, Rosell J, Galve JP, Carbonel D (2012) Investigating gravitational grabens related to lateral spreading and evaporite dissolution subsidence by means of detailed mapping, trenching, and electrical resistivity tomography (Spanish pyrenees). Lithosphere 4:331–353. doi:10.1130/l202.1
GVA (2017) Terrasit. Valencia,
Heckmann T, Bimböse M, Krautblatter M, Haas F, Becht M, Morche D (2012) From geotechnical analysis to quantification and modelling using lidar data: a study on rockfall in the reintal catchment, bavarian alps, germany. Earth Surf Process Landf 37:119–133. doi:10.1002/esp.2250
Hungr O, Leroueil S, Picarelli L (2014) The varnes classification of landslide types, an update. Landslides 11:167–194. doi:10.1007/s10346-013-0436-y
Hürlimann M, Copons R, Altimir J (2006) Detailed debris flow hazard assessment in andorra: a multidisciplinary approach. Geomorphology 78:359–372. doi:10.1016/j.geomorph.2006.02.003
Intelligent_Resources_Inc (2006) Manual for the software rayfract
ISRM (1978) Suggested methods for the quantitative description of discontinities in rock masses. Int J Rock Mech Min Sci Geomech Abstr 15:319–368
Jaboyedoff M, Oppikofer T, Abellán A, Derron M-H, Loye A, Metzger R, Pedrazzini A (2012) Use of lidar in landslide investigations: a review. Nat Hazards 61:5–28. doi:10.1007/s11069-010-9634-2
Lague D, Brodu N, Leroux J. 2013. Accurate 3D comparison of complex topography with terrestrial laser scanner: application to the Rangitikei canyon (N-Z). J Photogramm Remote Sens 82:10–26. doi:10.1016/j.isprsjprs.2013.04.009
Mansour M, Morgenstern N, Martin C (2011) Expected damage from displacement of slow-moving slides. Landslides 8:117–131. doi:10.1007/s10346-010-0227-7
Mantovani M, Devoto S, Forte E, Mocnik A, Pasuto A, Piacentini D, Soldati M (2013) A multidisciplinary approach for rock spreading and block sliding investigation in the northwestern coast of malta. Landslides 10:611–622. doi:10.1007/s10346-012-0347-3
Merritt AJ, Chambers JE, Murphy W, Wilkinson PB, West LJ, Gunn DA, Meldrum PI, Kirkham M, Dixon N (2014) 3d ground model development for an active landslide in lias mudrocks using geophysical, remote sensing and geotechnical methods. Landslides 11:537–550. doi:10.1007/s10346-013-0409-1
Naudet V, Lazzari M, Perrone A, Loperte A, Piscitelli S, Lapenna V (2008) Integrated geophysical and geomorphological approach to investigate the snowmelt-triggered landslide of bosco piccolo village (basilicata, southern italy). Eng Geol 98:156–167. doi:10.1016/j.enggeo.2008.02.008
Palenzuela JA, Marsella M, Nardinocchi C, Pérez JL, Fernández T, Chacón J, Irigaray C (2014) Landslide detection and inventory by integrating lidar data in a gis environment. Landslides:1–16. doi:10.1007/s10346-014-0534-5
Pasuto A, Soldati M (2013) 7.25 lateral spreading a2 - shroder, john f. Treatise on geomorphology. Academic Press, San Diego, pp 239–248
Radbruch-Hall D (1978) Gravitational creep of rock masses on slopes. In: Voight B (ed) Rockslides and avalanches natural phenomena developments in geotechnical engineering. Elsevier, Amsterdam, pp 608–657
Riquelme AJ, Abellán A, Tomás R, Jaboyedoff M (2014) A new approach for semi-automatic rock mass joints recognition from 3d point clouds. Comput Geosci 68:38–52. doi:10.1016/j.cageo.2014.03.014
Riquelme AJ, Tomás R, Abellán A (2016) Characterization of rock slopes through slope mass rating using 3d point clouds. Int J Rock Mech Min Sci 84:165–176. doi:10.1016/j.ijrmms.2015.12.008
Rosser N, Lim M, Petley D, Dunning S and Allison R (2007) Patterns of precursory rockfall prior to slope failure. J Geophys Res : Earth Surf 112: n/a-n/a. doi: 10.1029/2006JF000642
Royán M, Abellán A, Jaboyedoff M, Vilaplana J, Calvet J (2014) Spatio-temporal analysis of rockfall pre-failure deformation using terrestrial lidar. Landslides 11:697–709. doi:10.1007/s10346-013-0442-0
Sass O, Bell R, Glade T (2008) Comparison of gpr, 2d-resistivity and traditional techniques for the subsurface exploration of the öschingen landslide, swabian alb (germany). Geomorphology 93:89–103. doi:10.1016/j.geomorph.2006.12.019
Saval JM, Tomás R, Delgado J, Tenza A, Baeza F and Ivorra S (2009) Estudio de estabilidad de taludes en el municipio de finestrat (alicante). Universidad de Alicante, pp 242
Schultz-Ela DD (2001) Excursus on gravity gliding and gravity spreading. J Struct Geol 23:725–731. doi:10.1016/S0191-8141(01)00004-9
Sturzenegger M, Stead D (2009a) Close-range terrestrial digital photogrammetry and terrestrial laser scanning for discontinuity characterization on rock cuts. Eng Geol 106:163–182. doi:10.1016/j.enggeo.2009.03.004
Sturzenegger M, Stead D (2009b) Quantifying discontinuity orientation and persistence on high mountain rock slopes and large landslides using terrestrial remote sensing techniques. Nat Hazards Earth Syst Sci 9:267–287. doi:10.5194/nhess-9-267-2009
Travelletti J, Malet J-P, Samyn K, Grandjean G, Jaboyedoff M (2013) Control of landslide retrogression by discontinuities: evidence by the integration of airborne- and ground-based geophysical information. Landslides 10:37–54. doi:10.1007/s10346-011-0310-8
Travelletti J, Malet JP (2012) Characterization of the 3d geometry of flow-like landslides: a methodology based on the integration of heterogeneous multi-source data. Eng Geol 128:30–48. doi:10.1016/j.enggeo.2011.05.003

R. Tomás (✉) · M. Cano · A. Riquelme · A. J. Tenza-Abril · F. Baeza-Brotons · J. M. Saval
Departamento de Ingeniería Civil, Escuela Politécnica Superior,
Universidad de Alicante,
Alicante, Spain
e-mail: roberto.tomas@ua.es

A. Abellán
Geography Department,
University of Cambridge,
Cambridge, UK

A. Abellán · M. Jaboyedoff
Faculté des Géosciences et de l'Environnement,
Institute of Earth Sciences, Université de Lausanne,
Lausanne, Switzerland